

3D kinematics through the X-shaped Milky Way bulge [★]

S. Vásquez^{1,2,3}, M. Zoccali^{1,3}, V. Hill⁴, A. Renzini^{5,6}, O. A. González^{2,3}, E. Gardner⁷, Victor P. Debattista⁸, A. C. Robin⁷, M. Rejkuba⁹, M. Baffico¹, M. Monelli^{10,11}, V. Motta¹², and D. Minniti^{1,3,13,14}

- ¹ Departamento de Astronomía y Astrofísica, Pontificia Universidad Católica de Chile, Av. Vicuña Mackenna 4860, Santiago, Chile. e-mail: svasquez@astro.puc.cl; mzoccali@astro.puc.cl
- ² European Southern Observatory, Alonso de Cordova 3107, Santiago, Chile
- ³ The Milky Way Millennium Nucleus, Av. Vicuña Mackenna 4860, 782-0436 Macul, Santiago, Chile.
- ⁴ Laboratoire Lagrange UMR7293, Université de Nice Sophia-Antipolis, CNRS, Observatoire de la Côte d'Azur, BP4229, F-06304 Nice, France
- ⁵ INAF - Osservatorio Astronomico di Padova, vicolo dell'Osservatorio 5, 35122, Padova, Italy.
- ⁶ GEPI, Observatoire de Paris, CNRS UMR 8111, Université Paris Diderot, F-92125, Meudon, Cedex, France.
- ⁷ Institut Utinam, CNRS UMR 6213, OSU THETA, Université de Franche-Comté, 41bis avenue de l'Observatoire, 25000 Besançon, France
- ⁸ Jeremiah Horrocks Insitute, University of Central Lancashire, Preston, PR1 2HE, UK.
- ⁹ European Southern Observatory, Karl-Schwarzschild-Strasse 2, 85748, Garching, Germany.
- ¹⁰ Instituto de Astrofísica de Canarias, Calle Vía Láctea s/n, E-38205 La Laguna, Tenerife, Spain.
- ¹¹ Departamento de Astrofísica, Universidad de La Laguna, E38200 La Laguna, Tenerife, Spain.
- ¹² Departamento de Física y Astronomía, Universidad de Valparaíso, Avenida Gran Bretana 1111, Valparaíso, Chile.
- ¹³ Vatican Observatory, V00120 Vatican City State, Italy.
- ¹⁴ Departamento de Ciencias Físicas, Universidad Andres Bello, Santiago, Chile

Received; accepted

ABSTRACT

Context. It has recently been discovered that the Galactic bulge is X-shaped, with the two southern *arms* of the X both crossing the lines of sight at $l = 0$ and $|b| > 4$, hence producing a double red clump in the bulge color magnitude diagram. Dynamical models predict the formation of X-shaped bulges, as extreme cases of boxy-peanut bulges. However, since X-shaped bulges were known to be present only in external galaxies, models have never been compared to kinematical data for individual stars.

Aims. We study the orbital motion of Galactic bulge stars, in the two *arms* (overdensities) of the X in the southern hemisphere. The goal is to provide observational constraints to bulge formation models that predict the formation of X-shapes through bar dynamical instabilities.

Methods. Radial velocities have been obtained for a sample of 454 bulge giants, roughly equally distributed between the bright and faint red clump, in a field at $(l, b) = (0, -6)$. Proper motions were derived for all red clump stars in the same field by combining images from two epochs obtained 11 years apart, with WFI@2.2m at La Silla. The observed field contains the Globular Cluster NGC 6558, whose member stars were used to assess the accuracy of the proper motion measurement. At the same time, as a by product, we provide the first proper motion measurement of NGC 6558. The proper motions for the spectroscopic sub-sample are analyzed taking into account the radial velocities and metallicities measured from near-IR Calcium triplet lines, for a subsample of 352 stars.

Results. The radial velocity distribution of stars in the bright red clump, tracing the closer overdensity of bulge stars, shows an excess of stars moving towards the Sun. Similarly, an excess of stars receding from the Sun is seen in the far overdensity, traced by faint red clump stars. This is explained with the presence of stars on elongated orbits, most likely streaming along the arms of the X-shaped bulge. Proper motions for these stars are consistent with qualitative predictions of dynamical models of peanut-shaped bulges. Surprisingly, stars on elongated orbits have preferentially metal poor (subsolar) metallicities, while the metal rich ones, in both overdensities, are preferentially found in more axisymmetric orbits.

The observed proper motion of NGC 6558 has been measured as $(\mu_l \cos(b), \mu_b) = (0.30 \pm 0.14, -0.43 \pm 0.13)$, with a dispersion of $(\sigma_l \cos(b), \sigma_b) = (1.8, 1.7)$ mas/yr. Being the first PM measurement for this cluster.

Key words. Galaxy: bulge – Galaxy: kinematics and dynamics – Galaxy: structure – Galaxies: kinematics and dynamics – globular clusters: individual: NGC 6558

1. Introduction

With $\sim 10^{10} M_{\odot}$ in stars (Kent 1992) the Galactic bulge is, after the disk, the second most massive stellar component of the Milky Way. It is the only galactic bulge in which its individ-

ual stars can be resolved down to the bottom of the main sequence, allowing the construction of deep color-magnitude diagrams (CMDs), astrometric proper motions measurements, radial velocities and detailed chemical composition studies from medium and high resolution spectroscopy. Thus, the Milky Way bulge offers a unique opportunity to map the stellar content of a bulge, as summarized by age, metallicity and kinematical multivariate distributions. All together, this observational evidence should help us to reconstruct the formation history of the bulge,

[★] Based on observations taken with ESO telescopes at the La Silla Paranal Observatory under programme IDs 163.O-0741(A), 085.D-0143(A) and 385.B-0735(B); and with observations taken with the Magellan telescope at the Las Campanas Observatory.

hence identify the basic physical processes that have led to its present dynamical structure and stellar content.

At least three distinct processes have been envisaged for the formation of galactic bulges. An early formation by merging of gas-rich smaller galaxies, a process traditionally invoked for the formation of elliptical galaxies (Toomre 1977); a late formation via the secular growth of a bar instability in a pure stellar disk (e.g., Combes & Sanders 1981; Saha et al. 2010; Shen et al. 2010, and references therein); and, more recently, an early formation via clump instability, migration and central coalescence in a very gas-rich disk (e.g. Immeli et al. 2004; Förster Schreiber et al. 2006; Carollo et al. 2007; Elmegreen et al. 2008; Bournaud et al. 2009; Genzel et al. 2011). Moreover, secular processes driven by a bar may dynamically change a pre-existing non-rotating bulge into a boxy bulge with high cylindrical rotation (Saha, Martínez-Valpuesta & Gerhard 2012). The predominantly old stellar content of the bulge (≥ 10 Gyr, Ortolani et al. 1995; Zoccali et al. 2003; Clarkson et al. 2011) demands an early formation, hence favoring processes that are supposed to act at an early time. On the other hand, the proven bar shape of the Galactic bulge (Stanek et al. 1994; Dwek et al. 1995; Rattenbury et al. 2007; and references therein) clearly demands that some sort of disk and bar instability had taken place. Thus, it is quite natural to expect that a variety of processes may have contributed to the build up of the bulge.

Although there has been general agreement that the bulge is bar-shaped, some of its structural parameters are still under discussion. Its axial ratios appear to be close to 1:0.35:0.25 but its inclination angle w.r.t. the line of sight has been reported in the range between ~ 15 and 45 degrees, depending on the method to trace it (e.g., Binney, Gerhard & Spergel 1997; Dehnen 2000; Bissantz & Gerhard 2002; Benjamin et al. 2005; Babusiaux & Gilmore 2005; Rattenbury et al. 2007; Robin et al. 2012; and references therein). Star counts at longitudes $|l| > 7$ provided hints for the presence of a second, longer and thinner bar (e.g., Hammersley et al. 2000; Cabrera-Lavers 2007, 2008; López-Corredoira et al. 2007; Churchwell et al. 2009), which however has been interpreted as more likely being a component of the bar itself (e.g., Martínez-Valpuesta & Gerhard 2011; Athanassoula 2012).

More recently, McWilliam & Zoccali (2010) and Nataf et al. (2010) used star counts of red clump (RC) stars from the 2MASS (Skruskie et al. 2006) and OGLE-III (Szymanski et al. 2011) catalogs, respectively, to show that, along the $l = 0$ direction, for latitudes exceeding $|b| = 5$, the RC splits in two components, indicating the presence of two peaks in stellar density along the line of sight. McWilliam & Zoccali (2010) interpreted this feature as evidence for the Galactic bar being X-shaped, which was later confirmed by Saito et al. (2011) in a more quantitative analysis of 2MASS RC giants across a larger bulge area. In this context, the main bar is just seen as the inner part of the X-shaped bulge.

X-shaped bulges can be qualitatively produced by some dynamical models as peculiar boxy/peanut (B/P) structures (e.g., Athanassoula 2005; Martínez-Valpuesta, Shlosman & Clayton 2006; Debattista et al. 2006) and X-shaped isophotes have been observed in a few S0 galaxies. However, such models have not been compared with observations of velocities for samples of individual stars, nor have been fine-tuned to reproduce a bulge with the characteristics of the Milky Way bulge, at least in part due to lack of observational constraints. We are now beginning to collect kinematical data for a large number of stars in the Galactic bulge, thus setting constraints on the proposed formation mechanisms.

Proper motions (PMs) can be obtained for large samples of stars with relatively short exposure times, but a long time baseline and precise astrometry are required in order to reach the needed accuracy of a few mas/yr, corresponding to the bulge proper motion dispersion. A pioneer study based on photographic plates taken 33 years apart has yielded proper motions for ~ 400 stars in Baade's Window (Spaenhauer et al. 1992), later followed by Rich & Terndrup (1997) in the same field. Zoccali et al. (2001) used the WFPC2 camera on board the Hubble Space Telescope to measure the proper motion of the bulge globular cluster NGC 6553 as well as the bulge dispersion of proper motions in the same field, and so did Feltzing & Johnson (2002) for the bulge globular cluster NGC 6528. Vieira et al. (2007) measured proper motions in the Plaut Window at $(l, b) = (0, -8)$ whereas a large proper motion catalog based on OGLE-II data, extending over several fields mostly at $b = -4$, has been obtained by Sumi et al. (2004). This catalog was used by Rattenbury et al. (2007) to compare the PM distribution of RC stars with bulge formation models. Kuijken & Rich (2002) used the WFPC2 camera on board the Hubble Space Telescope to demonstrate that the bulge CMD can be decontaminated from the foreground disk stars based on the different proper motion distributions of bulge and disk stars. Following this approach, Clarkson et al. (2008, 2011) used two epoch ACS/HST data to derive a bona fide pure-bulge CMD for a field at $(l, b) \sim (1, -2.51)$, clean from disk contamination, demonstrating that the bulge consists of a predominantly old population of ≥ 10 Gyr, and confirming a similar conclusion by Ortolani et al. (1995) and Zoccali et al. (2003) who used a more crude or a statistical foreground decontamination, respectively.

Important constraints on the bulge formation mechanism come from radial velocity measurements (Rich 1988, 1990; Terndrup et al. 1995; Minniti et al. 1996; Sadler et al. 1996) especially when proper motions are available on the same field. In fact, Zhao et al. (1996) combined the proper motions by Spaenhauer et al. (1992) with the radial velocities from most of the above mentioned samples deriving 3D space velocities for a sample of 62 K giants, that showed a significant vertex deviation. This result, later confirmed by Soto, Rich & Kuijken (2007), indicates a bar-like structure for the Galactic bulge. With a complex, simultaneous analysis of the metallicity distribution function and kinematics of Baade's Window giants, Babusiaux et al. (2010) and Hill et al. (2011) demonstrated that the vertex deviation is mainly produced by the most metal rich stars which have disk-like α -element abundance (Gonzalez et al. 2011), while the metal poor, α -enhanced stars have a kinematics more typical of a classical spheroid. The BRAVA survey (Howard et al. 2008, 2009; Kunder et al. 2012) obtained radial velocities for a total of $\sim 10,000$ bulge M giants in several fields spanning a wide range in longitude ($-10 < l < +10$) and latitudes ($b = -4, -6$ and -8), finding evidence for a cylindrical rotation. By comparing those data with their simple N-body model, Shen et al. (2010) argued for the Milky Way being a pure disk galaxy, i.e., without the need of a merger made bulge. It should be emphasized that the vast majority of early-type galaxies (over $\sim 86\%$, cf. Emsellem et al. 2011) are actually *fast rotators*, with just the most massive elliptical galaxies being predominantly *slow rotators*. Thus, the cylindrical rotation of the bulge does not necessarily imply a formation mechanism radically different from that of the majority of early-type galaxies.

A different approach of combining metallicity with radial velocity measurements has been followed by Rangwala et al. (2009a,b) who used Fabry-Perot imaging to sample the Calcium II Triplet (CaT) lines for $\sim 3,400$ stars along the bar ($l = 0, \pm 5$)

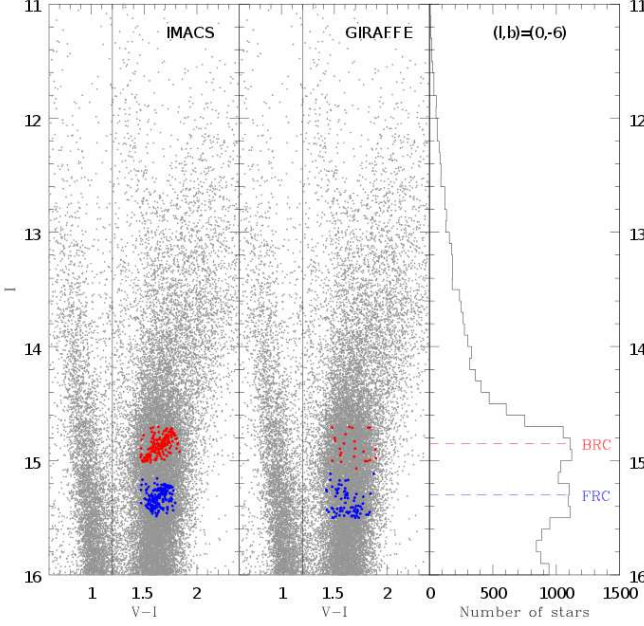


Fig. 1. Left and middle panels: Optical color magnitude diagram of the bulge field at $(l, b) = (0, -6)$ obtained with WFI@2.2m at La Silla. The vertical line marks the color cut applied to construct the histogram on the right ($V - I > 1.2$), where the two clumps are clearly visible. The Bright Red Clump (BRC – red points) and Faint Red Clump (FRC – blue points) spectroscopic target selection observed with IMACS on Magellan and with FLAMES-GIRAFFE on VLT are overlotted on the CMD in the left and middle panels, respectively.

at $b = -4$. They detected the presence of bar stellar streaming motions along the spanned longitudes. Radial velocities and metallicities separately for bright and faint red clump stars were first obtained by de Propris et al. (2011) in a bulge field at $(l, b) = (0, -8)$, and more recently by Uttenhaler et al. (2012) in a field at $(l, b) = (0, -10)$, and by Ness et al (2012) in three fields along the minor axis at $b < -5$.

In the present paper we combine radial velocity and proper motion measurements to derive the 3D motion of 454 bulge stars in the bright and faint red clump of a field at $(l, b) = (0, -6)$. Like those in the de Propris et al. study, these stars trace the near and far *arms* of the X-shaped bulge, respectively. The paper is organized as follows. In Section 2 we describe the data and reduction methods for our photometric, astrometric and spectroscopic measures, whereas in section 3 and 4 the resulting radial velocities and proper motions are presented. In section 5 are presented the space velocities. The metallicity distributions of the stars in the two red clumps are presented in Section 6, and conclusions are drawn in Section 7.

2. Observations and Data Reduction

2.1. WFI Photometry

The spectroscopic targets were selected based on the optical V, I photometry of a bulge field centered at $(l, b) = (0, -6)$, obtained with the WFI camera at the 2.2m telescope at ESO La Silla, on April 15th, 1999 as part of the ESO imaging Survey ESO programme (EIS, ESO programme ID 163.O-0741(A)). The resulting CMD has been already presented in Zoccali et al. (2003) and

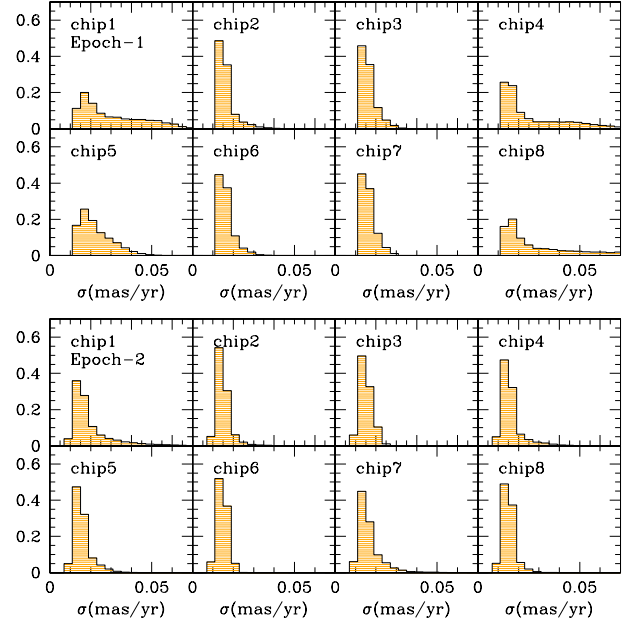


Fig. 2. The dispersion of the position (X, Y) of the stars in every frame, for each epoch, is plotted across the WFI detector in units of mas/yr . A higher spread in the dispersion is observed in the edges of the CCD associated with higher order distortion and variable PSF. All of this effects are mostly corrected in the procedure done in the astrometrization (see text for details).

McWilliam & Zoccali (2010). Figure 1 shows the bright portion of the CMD, which clearly displays double red clump, as illustrated in the right panel. Given the modest dependence of the red clump magnitude on stellar population properties (age and metallicity), McWilliam & Zoccali concluded that the two clumps trace two stellar overdensities at different distances along the line of sight, and that these overdensities correspond to the near and far arm of the X-shaped bulge. Based on this CMD the red clump targets were selected among the bright (red dots) and faint red clump stars (blue dots) for spectroscopic follow-up with Magellan IMACS and VLT FLAMES-GIRAFFE spectrographs.

In order to derive space velocities for our targets, second epoch images of the same field were obtained on May 6th, 2010 with the same instrument and filters as in the first epoch (ESO programme ID 085.D-0143(A)). Thus, images were taken through the V - and I -band filters, with integration times of $7 \times 50s$ for both. While the seeing of the first epoch was excellent (0.6–0.7 arcsec, observed at airmass=1.06), the second epoch had average seeing 1.6 arcsec, at airmass=1.19. Photometry was carried out with the DAOPHOTII/ALLFRAME packages (Stetson 1988, 1994), on individual chips, while the photometric calibration was derived by comparison of stars with the first epoch.

2.2. WFI Astrometry

The X, Y coordinates for each star were determined in each individual exposure (hereafter *frame*), in each epoch. We used 7 frames in the first epoch (3 V and 4 I , see Zoccali et al. (2003) for details) and 14 frames in the second epoch (7 in V and I). The set of codes developed by P.B. Stetson (DAOMATCH and DAOMASTER; Stetson, private communication) were used to transform the coordinates of each star in each frame into the sys-

tem of the reference frame of each epoch. A cubic transformation was allowed among different frames of each epoch, in order to properly take into account distortions at the edges of the chips. Different effects contribute to the distortions among different frames and between the two epochs. Among them, the non perfect alignment among the chips of the WFI mosaic shown in Fig. 2.7 of the WFI Handbook (version 2.2, March 2013) and the differential atmospheric refraction described in Filippenko (1982). Following Filippenko, we calculated the effect of atmospheric refraction, at the central wavelengths of the V and I filters, at the center of the detector and at one edge (15 arcmin away). The differential shift between the center and the edge varies by 0.002 arcsec between the two filters, at the airmass of epoch1 and by 0.0025 arcsec at the airmass of epoch2. This values would not be completely negligible in our case, because it corresponds to 0.01 pixels. However, this effect has been removed by the cubic coordinate transformation performed to each chip. An atmospheric effect that can not be corrected by our procedure is the atmospheric dispersion. Due we are using broad band filters, the refracted light from a star will be dispersed along the parallactic angle producing a small spectra instead a point source image on the detector, where the maximum of the light distribution will depends on the color of the star. This fact will affect the determination of the spatial centroid, especially for stars with large color difference. In order to estimate this effect we compute the differential atmospheric refraction like above, for two stars with effective temperature of $T_{eff} = 4500$ K and $T_{eff} = 6000$ K (which correspond with a typical RC and MS star). The comparison shows that for both filters, the differential shift between the two stars are quite small, reaching 0.001 mas/yr for V band and less than 0.0001 mas/yr for I band. This scatter on the coordinates determination can not be corrected, but it is so small that will no affect our analysis.

The final catalogue for each epoch was then obtained by averaging the positions of each star, in all the frames in which it was detected. Stars in the magnitude range of interest here ($I < 16$) were detected in all the frames of the two epochs, with very few exceptions. An indication of the relative precision of our astrometry is given by the standard deviation, σ , of the position of a given star in different frames. This is shown in Fig. 2, where histograms of $\sigma = (\sigma_x^2 + \sigma_y^2)^{1/2}$, in units of *mas/yr* are plotted for every WFI chip, in both epochs. The dispersion is extremely small for all chips, typically within 0.05 mas/yr, corresponding to 0.002 pixels. We can reach this small dispersion because the photometry has been done with ALLFRAME, a code that “makes simultaneous use of the geometric and photometric information from all the frames of a given field to derive a self-consistent set of positions and magnitudes...” (Stetson 1994). In other words, the dispersion in Fig. 2 is very small because the individual measurements are not completely independent. Yet, it gives an estimate at least of the relative precision in different parts of the mosaic. The figure also shows that the dispersion at the edge of the mosaic (chip #1,#4,#5 and #8) is higher than in the middle, because of the higher order distortion and variable PSF. This effect is larger in the first epoch, most likely due to the smaller number of frames and because the stellar profiles here are slightly undersampled, due to the excellent seeing conditions.

The astrometrization of the final X, Y catalogues was done by means of the IRAF routines *ccymatch*, *ccmap* and *cctran*. A 7-order polynomial transformation was adopted, and the PPMXL catalog (Roeser et al. 2010) was used as reference. The two astrometrized WFI catalogs were then matched using the *topcat* catalog-handling package (Taylor 2005), but the residuals

showed trends and steps mostly corresponding to the edges of the individual chips. These trends did not disappear by changing the order of the astrometric solution, and they were even larger if the UCAC3 catalogue (Zacharias et al. 2010) was used as reference instead of the PPMXL. A more complex procedure was then adopted to eliminate these residual trends.

First, an astrometric solution (7th order polynomial for each chip) was found in order to convert (X_1, Y_1) to (RA_1, DEC_1) and (X_2, Y_2) to (RA_2, DEC_2) . This was done using only bulge RGB stars¹ and the PPMXL catalogue as reference. The two RA, DEC catalogs were then matched to each other. Residual trends were present, as discussed above, but this matched catalogue was used only as a first step, to combine the chips in a single mosaic and have the star pairs in hand.

A new transformation was then derived between pixel coordinates of star pairs in the two epochs, (X_1, Y_1) and (X_2, Y_2) , and it was applied to the latter, to bring them to the pixel coordinate system of the 1st epoch (X_1^1, Y_1^1) . For this transformation, in order to avoid adopting a high order polynomial that could *flare* at the edges of the chips, we preferred to divide the field in small boxes 300×300 pixel wide (71×71 arcsec), and impose a first order transformation (a plane) in each subfield. Finally, both (X_1, Y_1) and (X_2^1, Y_2^1) were transformed to (RA, DEC) using the *same* astrometric solution found in the first step, for epoch 1 only. This last step ensured that any spurious trend in the astrometric solution was applied to the pixel coordinates of both epochs, which was effective in removing completely the trends in the residual differences between the coordinates of the two epochs, thus allowing us to minimize the proper motion error. The final (RA, DEC) of both epochs were transformed into galactic coordinates (l, b) by means of the *topcat* package.

2.3. IMACS spectra

Spectra for 177 bright RC stars and 175 faint RC stars were observed with the multi slit mode of the IMACS spectrograph at the Las Campanas Observatory on July 10th, 2010. A 1200 lines/mm grating was used, with a blaze angle of 26.7 degrees. This setup produces spectra centered at ~ 8500 Å (the precise value depending on the position of the star in the field of view) with a resolution $R \sim 5000$. The spectra have S/N \sim 40 in the Calcium Triplet (CaT) region, yielding velocities accurate to a few km/s.

The spectra were reduced using the COSMOS pipeline, provided by The Carnegie Observatories. This pipeline processes the multi slit spectra from IMACS applying bias and flat field corrections, wavelength calibration and sky subtraction to each 2d-spectrum. The final extraction to 1d-spectra and velocity measurement was done with IRAF *apall* and *fxcor* tasks. As a test for the wavelength calibration made for COSMOS, the sky lines in each spectra were cross-correlated with a sky lines template from UVES (Hanuschik 2003). The residual shifts found ($\sim |10|$ km/s) were applied to individual spectra in order to set them at the geocentric rest frame.

The radial velocities of our sample were measured by cross-correlation against a synthetic spectral template for a typical RGB star with $T_{eff} = 4750$ K and $[Fe/H] = -1.3$ covering the region from 8350 Å until 8950 Å, where the CaT lines are located. Due the IMACS CCD mosaic configuration, with 8 chips in a square array separated by gaps, in a few spectra one of the three lines fell in the gap. In such cases the measurement was made

¹ Only stars with $V - I > 1.4$ and $V < 18.5$ were used, and the disk red clump sequence sticking out from the bulge RGB, at $V - I = 1.6$, $V = 15$ upward and to the blue, was also excluded.

using only the available section in the spectra and the respective range in the template. The typical error obtained from the cross-correlation was ~ 2.0 km/s without significant outliers ($\sigma \sim 0.8$ km/s). Finally, heliocentric corrections were calculated with the IRAF task *rvcorrect* and applied to all radial velocities.

2.4. FLAMES-GIRAFFE spectra

Red clump stars in the same field at $(l, b) = (0, -6)$ were also observed with the multi-fibre FLAMES-GIRAFFE spectrograph at the VLT in Medusa mode within the ESO programme ID 385.B-0735(B) in service mode. Spectra were taken with the LR08 setup, centered at 8817 \AA yielding a spectral resolution of $R=6500$ and average $S/N \sim 50$. These observations were not especially fine tuned to discriminate between the two RCs, and therefore the target stars were not evenly distributed between the two RCs. Of 130 Medusa fibres 24 were allocated to the bright RC, and 78 to the faint RC stars. The middle panel in Figure 1 shows the FLAMES-GIRAFFE target selection in the CMD.

GIRAFFE spectra were extracted and wavelength calibrated with the instrument pipeline available from ESO, and radial velocities were measured via cross-correlation with IRAF *fxcor* task, using the same template set as for IMACS spectra. As expected by the difference in resolution as well as from the usage of fibre vs. slit spectrograph, the typical error for GIRAFFE radial velocity measurements was smaller than for IMACS observations (V_{Helio} error ~ 1 km/s with dispersion ~ 0.3 km/s).

There are four stars in common between IMACS and GIRAFFE observed data set. These stars have a mean difference on measured radial velocity of $\Delta V_{\text{Helio}} \sim 4 \pm 2$ km/s, and were used to measure the systematic difference in $[\text{Fe}/\text{H}]$ for both samples (Sect. 6).

3. Radial Velocities for bulge Red Clump stars

Figure 3 (top) shows the cumulative heliocentric radial velocity (RV) distribution for the RC stars obtained in this work, compared with the sample of K giants stars analysed in Zoccali et al. (2008; see also Babusiaux et al. 2010) and with the sample of M giants observed within the BRAVA survey (Kunder et al. 2012). The three samples were obtained in the same field at $(l, b)=(0, -6)$, and the number of stars in each sample is indicated in the labels. According to a Kolmogorov-Smirnov test, RC stars and M giants have the same RV distribution, with a confidence of 71%. On the other hand, K giants, selected in a box located at ~ 0.75 mag above the RC, have a RV distribution more peaked towards $V_{\text{Helio}} = 0$ km/s, that is different from that of RC stars with a confidence of 89%. This difference is also clear if we measure the RV dispersion of the two samples: $\sigma_{\text{RC}} = 97 \pm 4$ km/s versus $\sigma_{\text{K}} = 83 \pm 4$ km/s. The RV dispersion of M giants from the BRAVA sample, instead, is $\sigma_{\text{M}} = 101 \pm 5$ km/s, within 1σ of that of RC stars.

One possible explanation for the difference between the RV distribution of RC and K giants, in this field, is a different amount of contamination by foreground disk stars, expected to have a RV distribution peaked at $V_{\text{Helio}} = 0$ km/s. Indeed, the disk RC at different distances and reddenings, along the line of sight, is clearly visible in the CMD of Figure 1 as a diagonal sequence parallel to the disk MS, but shifted ~ 1 mag to the red. This sequence intersects the bulge RGB precisely between $I = 14$ and $I = 14.5$, which are the magnitude limits of the K giants target box (c.f., Figure 1 in Zoccali et al. 2008). On the contrary, M giants in the BRAVA sample were selected such

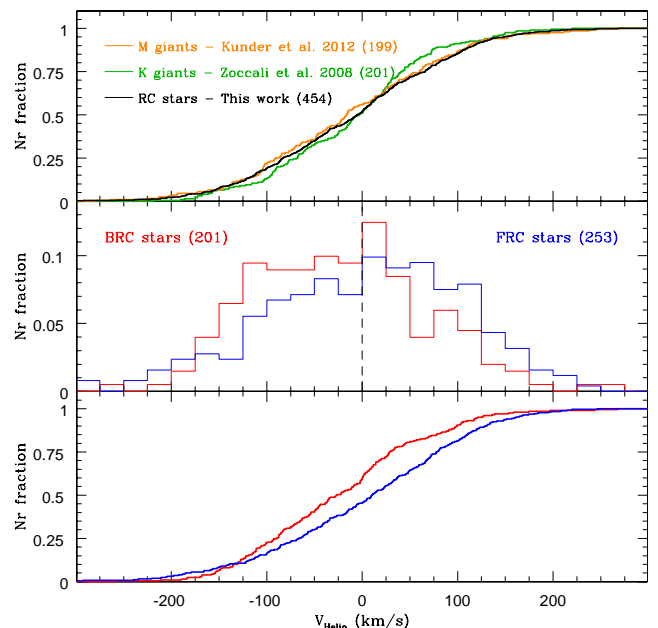


Fig. 3. Upper panel: cumulative distributions of the heliocentric radial velocities for bulge stars in the RC (black; this work), K giants (green; Zoccali et al. 2008) and M giants (orange; Kunder et al. 2012). All the stars are located in the same field at galactic coordinates $(0, -6)$. A Kolmogorov-Smirnov test shows that RC stars and M giants have radial velocity distributions that are similar, with a confidence of 71%. On the contrary, K giants have a radial velocity distribution that is more peaked at $V_{\text{Helio}} = 0$ km/s with 89% confidence of being *different* from RC stars. See text for discussion. Middle and lower panels: Histograms and cumulative distributions for heliocentric radial velocities of bulge stars in the bright and faint RC, respectively. The two distributions differ from each other, with a confidence of 99.95%, according to the Kolmogorov-Smirnov test.

as to avoid the disk RC sequence, while bulge RC stars largely outnumber the disk foreground stars, in the same CMD box, because they indeed *clump* at that magnitude.

The middle and lower panels of Figure 3 show respectively the differential and cumulative heliocentric RV distribution of stars in the bright and in the faint RC. Both the IMACS and GIRAFFE target stars are included in the histograms. The Kolmogorov-Smirnov test yields a confidence of 99.95% that the two distributions are different. In fact, it is visually evident that there is an excess of stars with $V_{\text{Helio}} \sim -80$ km/s in the bright RC sample, while a similar excess is visible at $V_{\text{Helio}} \sim +80$ km/s in the faint RC sample. A dashed line at $V_{\text{Helio}} = 0$ km/s has been drawn in these panels to visually emphasize the asymmetry of the two distributions.

Before trying to understand the observed asymmetry in the RV distribution of the two clumps, it is worth considering two sources of contamination. First of all, we know that foreground disk RC at distances $d > 5$ kpc from the Sun would fall into the CMD selection boxes. These stars should have RV close to zero, and a narrower velocity dispersion, especially those closer to the Sun, contaminating the bright RC. According to the Besançon model of the Galaxy (Robin et al. 2003), the contamination from disk foreground stars should be small for both RCs (3% and 8% by thin and thick disks respectively). The density of both disks in

the inner few kpc of the Galaxy, however, has never been constrained observationally, so the model predictions are extremely uncertain on this point. Recently, the Besançon model has been updated (Robin et al. 2012) including two populations in the inner bulge, and despite the differences with the old model (both for the bulge component but also the adjustments to the discs, most notably the thick disc), the figures for the contaminations are similarly low: 3% and 7% contamination from the thin and thick disc, respectively, for the BRC. While a contamination of 4% and 7% were estimated for the FRC. In order to estimate the contamination fractions quoted above we split (arbitrarily) the single RC predicted in two components, each one containing half of the bulge RC stars, and counted the model disk stars in two boxes with the magnitude and color limits of our spectroscopic targets. Overall, we can expect that the stars at RV close to zero might suffer from some degree of disk contamination, hard to quantify here.

A second source of contamination comes from the bulge RGB stars in the two overdensities along the line of sight, because the upper RGB stars of the far arm (that corresponds to the faint RC) overlap the bright RC, whereas the lower RGB stars of the nearby arm contaminate the faint RC selection box. Furthermore, other bulge stars not associated with the two arms (overdensities) might also exist along the line of sight.

All together, these contaminations and cross-contaminations act in such a way that each selection box on the CMD will not include purely stars at the distances of the overdensities identified by the two RCs, with the effect of smoothing the features of the two RV distributions seen in Figure 3, and making them more similar to each other than they actually are.

An estimate of the fraction of RGB stars included in each of the two RC boxes has been calculated by generating a synthetic CMD from the BASTi library of stellar models, assuming an age of 10 Gyr and solar metallicity. Then the cross-contamination has been evaluated considering the 0.5 mag difference in distance modulus (~ 2 kpc) between the two overdensities and counting the fraction of RGB and RC stars that fall in each selection box. After rescaling these two fractions by taking into account the cone effect, we finally estimated a cross-contamination fraction of $\sim 18\%$ in both RCs.

It is important to note that the above mentioned effects, namely foreground and cross-contamination, are *certainly* present, even if their impact is hard to precisely quantify here. This consideration supports the assumption, that we make in the following analysis, according to which the near arm is dominated by stars with mostly negative radial velocities, roughly centered at $V_{\text{Helio}} = -80$ km/s, whereas the far arm is dominated by stars with mostly positive radial velocities, roughly centered at $V_{\text{Helio}} = +80$ km/s.

4. Proper Motions

In order to assess the precision of the proper motions derived as described in Section 2.2 we took advantage of the presence in our $(l, b) = (0, -6)$ field of the globular cluster NGC 6558. To this end, we select the stars within a radius of 2 arcmin from the cluster center (Half-light radius ~ 2.15 arcmin, taken from Harris 1996). Due to the lower metallicity of NGC 6558 ($[\text{Fe}/\text{H}] = -0.97 \pm 0.15$) with respect to the bulge, it is possible to select a clean sample of clusters stars from the observed CMD selecting stars on the upper RGB ($I < 16.5$) that are bluer than the bulge RGB. Cluster stars are expected to have an internal velocity dispersion of ~ 10 km/s (Pryor & Meylan 1993), that, at the distance of NGC 6558 corresponds to

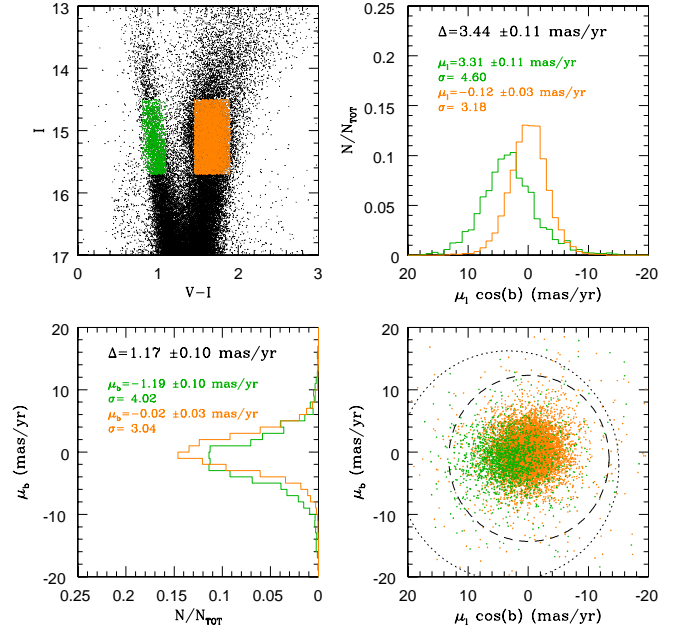


Fig. 4. Proper motions measured at $(l, b) = (0, -6)$ field. RGB bulge stars and disk dwarfs are shown with orange and green colors respectively. Dotted and dashed circles in μ_1 vs μ_b plot show the 3σ data selection used for disk and bulge stars, respectively. The proper motion distribution derived from this selection show a systematic difference between disk and bulge population, in agreement with Clarkson et al (2008).

a proper motion dispersion of 0.3 mas/yr, too small to be measured here. Therefore, we attribute the observed dispersion of cluster stars completely to observational errors. After a 3 sigma-clipping, cluster stars show an observed mean proper motion of $(\mu_1 \cos(b), \mu_b) = (0.30 \pm 0.14, -0.43 \pm 0.13)$, with a dispersion of $(\sigma_1 \cos(b), \sigma_b) = (1.8, 1.7)$ mas/yr. The latter is, therefore, the observational error we will use to deconvolve the observed proper motion dispersion of bulge stars. Note that this is an upper limit to our real error, because cluster stars are more crowded than bulge stars, and because NGC6558 happens to fall at the edge of chip #6.

Another test to assess the accuracy of our catalogue is to separate a pure disk population, selected on the blue main sequence in the CMD (as shown in Figure 4) and the bulge population selected along the RGB near the RC. The proper motion diagram for these two samples, in galactic coordinates, shows that there is a difference between the mean PM of the disk and bulge populations. After applying a 3-sigma clipping to both distributions, the disk-bulge offset was found to be $(\Delta\mu_1 \cos(b), \Delta\mu_b) = (3.44 \pm 0.11, 1.17 \pm 0.10)$ mas/yr, which compares favourably to $(3.21 \pm 0.15, 0.81 \pm 0.13)$ found by Clarkson et al. (2008) in a field at $(l, b) = (1.25, -2.65)$. Additionally, if we deconvolve the bulge proper motion dispersion from the observational error as estimated above, we obtain $(\sigma_1 \cos(b), \sigma_b) = (2.62, 2.52)$ mas/yr, in excellent agreement with the values of $(\sigma_1 \cos(b), \sigma_b) = (2.64, 2.40)$ mas/yr measured by Rattenbury et al. (2007) in two fields at $(l, b) = (-0.25, -5.70)$ and $(l, b) = (-0.14, -5.91)$.

The two epoch images analyzed here had not been obtained with the purpose of deriving proper motions. Therefore the observational strategy (dithering, etc.) was not optimized for this kind of study. Nevertheless, the measurements reported above

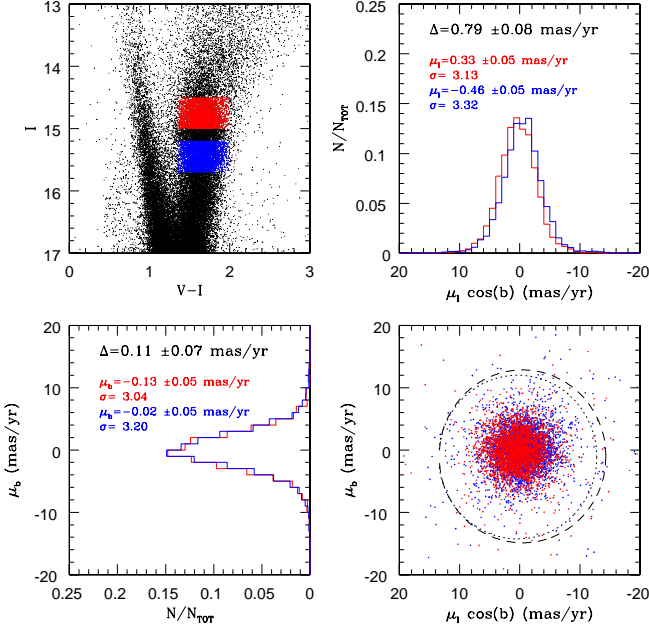


Fig. 5. Proper motion measured at $(l, b) = (0, -6)$ field for bulge RC stars. The blue and red dots identify the selected bright RC (BRC) and faint RC (FRC) stars on the CMD, respectively. A 3σ selection (lower right panel) in μ_l and μ_b plane is used to define the sample further analysed with histograms. Lower left panel shows μ_b distribution, while upper right panel compares μ_l distributions for the bright (red) and faint (blue) RC stars. The mean values of μ_l and μ_b for the BRC and FRC samples are given in the respective panels showing the distributions, and we also provide the mean differences in proper motion for the two RC populations.

confirmed that the derived proper motions, although not very precise, should be good enough to allow us to identify differences in the mean proper motion of the two bulge overdensities traced by the bright and faint RCs.

The proper motion of stars in the two RCs is shown in Figure 5. The bright RC contains stars with $14.5 < I < 15.0$ and $1.35 < V - I < 2$, while the faint RC stars have $15.2 < I < 15.7$ and $1.35 < V - I < 2$ as illustrated in the upper/left panel of Figure 5, where the two groups have approximately the same number of stars. There is a small but statistically significant shift $\Delta\mu_l \cos(b) = 0.79 \pm 0.08$ mas/yr in the longitude proper motions between the two distributions ($\sim 100\%$ confidence from a KS test), whereas the two latitude proper motion distributions are instead barely distinguishable.

For the spectroscopic targets it is possible to combine the information from the PMs with that from RVs, thus deriving 3D space velocity for individual stars. The upper panels of Figure 6 show that both bright and faint RC stars share a common trend in μ_l vs V_{Helio} which is not observed in μ_b (Pearson correlation coefficient of ~ -0.2 and ~ 0.05 , respectively). To emphasize this behaviour a linear regression between PMs and RV was calculated for each sample and over-plotted on the data points.

Following the arguments given in Section 3, the cleanest sample of bright RC stars is the one with negative radial velocities, while the cleanest sample of faint RC stars has positive radial velocities. If these arguments are correct, then the stars we want to probe should be at the extreme of the two radial veloc-

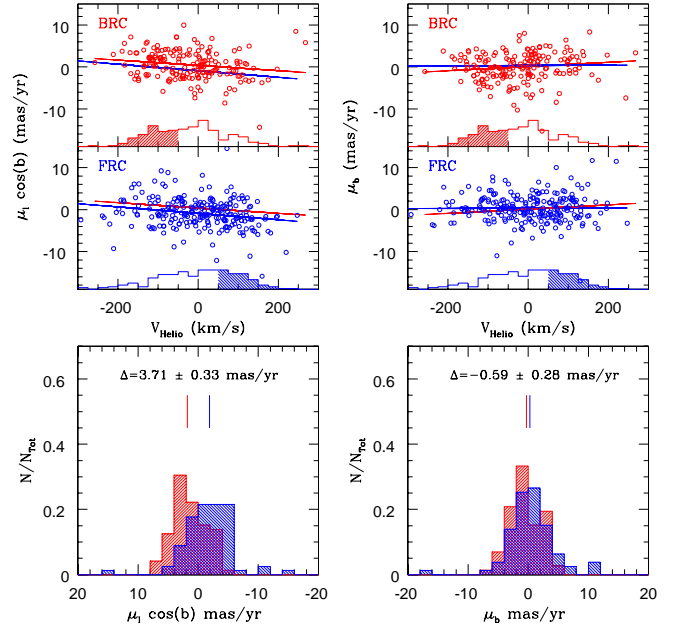


Fig. 6. Upper panels: PMs versus RVs for BRC and FRC sample. Colour lines (red for BRC and blue for FRC) shows the linear regression for our data in the respective sample. As is shown in the right-upper panel, no significant difference in μ_b versus RV is observed, while for μ_l a common trend with RV is found (left/upper panel). Under each scatter plot is also shown the scaled RV distribution for each sample, in order to define a *pure* BRC and FRC samples (red and blue dashed regions, respectively). Lower panels: Histograms for observed proper motions and the difference in the median for selected stars in each *pure* sample defined above.

ity distributions. Arbitrary selections of stars with $V_{\text{Helio}} < -50$ km/s and $V_{\text{Helio}} > +50$ km/s were made to the bright and faint RCs, respectively, and they are shown at the bottom of each scatter plot, where small versions of the RV distributions are also shown. The PMs of these stars are compared in the two lower panels in the same figure, showing a significant offset in μ_l , while the mean μ_b values are virtually identical.

These results can be interpreted as follows. In the near and far overdensities, we observe stars on radial orbits (V_{Helio} non-zero). An excess of stars approaching the Sun is present in the near overdensity, while an excess of stars receding from the Sun is present in the far overdensity. By itself, this is an indication of stars in streaming motions along the *bar*. In our bulge the *bar* has been proved to be X-shaped. Structures of this kind have been proposed to form by buckling and bending of the stellar distribution where stars are re-arranged on banana-orbits, i.e., the family of $x1v1$ orbits according to Patsis, Skokos & Athanassoula (2002), that look either like a ‘frown’ (\frown) or a ‘smile’ (\smile) when viewed edge on. This is the main family of stable, periodic orbits forming a peanut-shaped, or an X-shaped bulge.

Stars near the velocity inversion points of such orbits, which are the ones that we are probing at $b = -6$, are expected to go in opposite radial, as well as opposite longitude directions, if, as in our case, the line of sight crosses two opposite sides of the

orbit². On the contrary, since both overdensities, at this latitude, lie below the plane, they are expected to share a common mean μ_b , as observed.

Our result differs from that of De Propris et al. (2011), who found no differences between the RV distribution of bright and faint RC stars in a fields at $b = -8$. Although we do not have a conclusive explanation for this discrepancy, a few factors can account for at least part of it. De Propris et al. (2011) have selected their targets from the 2MASS CMD. It is clear from their Figure 1 that they have larger contamination from disk main sequence stars in the faint RC, and possibly also from the bright RC (due to the larger error on individual magnitudes of 2MASS versus WFI photometry). A slightly larger error on the magnitudes of individual stars in 2MASS versus WFI photometry, and a slightly larger error on the radial velocities (from their lower S/N and lower resolution spectra) might also contribute to mask out the features we found in the faint RC distribution.

Radial velocities for stars in the two RCs visible on the bulge minor axis were recently derived also by Uttenthaler et al. (2012) and Ness et al. (2012). The latter compares the measured distributions with the prediction of a bulge model by Athanassoula (2003). The model was not optimized to reproduce the Galactic bulge, hence cannot be taken quantitatively, but it is a model of a peanut shaped bulge that, at least qualitatively, reproduces the two observed overdensities along the lines of sights on the minor axis. The model predicts the presence of a clear asymmetry, in the radial velocity distribution at $b = -5$, similar to the one observed by Ness et al. (2012) at this latitude, and to the one presented here. At larger latitudes, however, the asymmetry becomes much weaker in the model, and also in the observations by Ness et al. (2012) at $b = -7.5$ and $b = -10$. The fact that the asymmetry is predicted to weaken at high latitudes might, perhaps, explain the similarity between the RV distributions of bright and faint RCs observed by de Propris et al. (2010) and Uttenthaler et al. (2012).

We can conclude that we have identified stars, in the near and far overdensities of the lower part of the X-shaped bulge, whose 3D kinematics are qualitatively consistent with the prediction of dynamical models producing a peanut-shaped, or an X-shaped, bulge from the buckling instability of a bar. These are not *all* the stars we see in the near and far overdensities traced by the near and far RCs. In each of the two RCs there are indeed also stars sharing the same 3D velocities, as well as a small number of stars with radial velocities opposite to the main stream. These can be qualitatively interpreted as stars in more stochastic (spheroid-like) orbits, plus some degree of cross contamination (cf Section 3).

5. Space Velocities

Space velocities were obtained for all the spectroscopic targets, in the U, V, W Galactic Cartesian system following Johnson & Soderblom (1987), assuming that stars in the bright and faint RC are on average at a distance of 6.5 and 8.5 kpc from the Sun, respectively. Because our proper motions are relative to mean position of the bulge stars instead of quasars or distant galaxies, it is necessary to correct them by the relative motion of the galactic center with respect to an inertial frame before computing U ,

² The line of sight at $(l, b)=(0, -6)$ intercepts the two overdensities formed by the family of *frown*-like orbits. In particular, it touches the West side of the near part of the *frown*, and the East side of the far one.

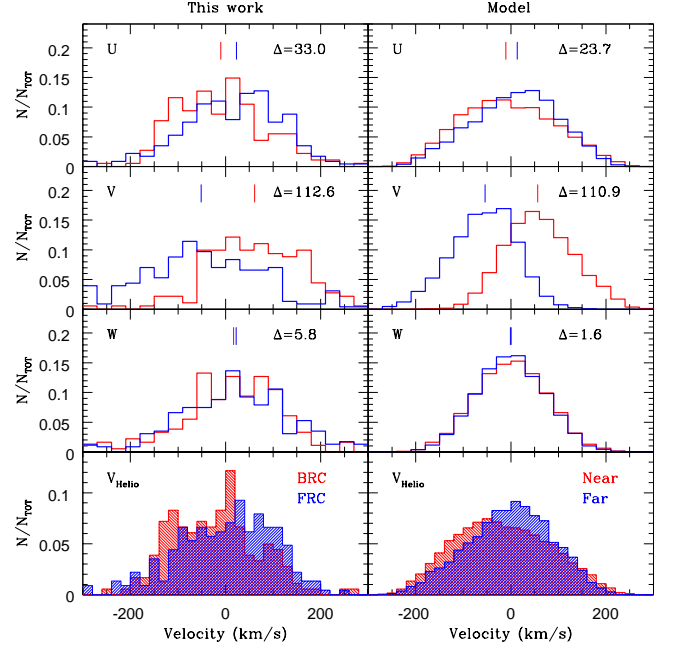


Fig. 7. BRC and FRC are compared with respect the kinematical model for a strong Boxy–Peanut bulge (Debattista et al. 2005). From the model, two samples were selected around the two overdensities formed by the Near (red) and Far (blue) arms of the Boxy–Peanut stellar distribution, in the line of sight for $(l, b)=(0, -6)$. Colour lines over U, V and W histograms correspond to the median value for each distribution.

V and W velocities. Sumi et al. (2004) determine this correction as:³

$$\mu_{\alpha^* \text{INERT}} = \mu_{\alpha^* \text{OBS}} - \mu_{\alpha^* \text{GC}} + \mu_{\alpha^* \text{GC,INERT}} \quad (1)$$

$$\mu_{\delta \text{INERT}} = \mu_{\delta \text{OBS}} - \mu_{\delta \text{GC}} + \mu_{\delta \text{GC,INERT}} \quad (2)$$

where the subscript OBS and GC refer to observed PM of individual stars and the mean PM of the galactic bulge respectively. The quantities $(\mu_{\alpha^* \text{GC,INERT}}, \mu_{\delta \text{GC,INERT}}) = (-2.93, -5.17)$ mas/yr correspond to the expected motion of the galactic center with respect to the inertial frame. The spatial velocities were corrected from the peculiar solar motion $(u, v, w)_{\odot} = (11.1, 12.24, 7.25)$ km/s (Schönrich, Binney and Dehnen 2010), considering the solar circle radius and Local Standard of Rest as $R_{\text{GC}} = 8.0$ kpc and $\text{LSR}_{\odot} = 220$ km/s respectively. We adopted the usual notation where U is the radial component along the star-Galactic center direction, positive towards the Galactic center; V is the peculiar rotational velocity of each star with respect to its Local Standard of Rest, positive in the sense of the Galactic rotation; W is the vertical velocity component, positive towards the North Galactic pole.

5.1. Model Comparison

We compare our observations to the high resolution model R1 of Debattista et al. (2005). Here we briefly describe this model and the method we used for comparing with the observational data. This model starts out with an exponential disk with a ratio of scale-height to scale-length, $z_d/R_d = 0.05$. The disk has

³ $\mu_{\alpha^*} = \mu_{\alpha} \cos \delta$

Table 1. Statistics for velocities presented in Fig. 7, in km/s.

	V_{Helio}	U	V	W	V_{Helio}	U	V	W
	BRC ($N = 181$):				FRC ($N = 227$):			
Mean	-22.3 ± 6.9	-10.0 ± 7.0	65.9 ± 8.2	13.8 ± 8.4	1.0 ± 6.7	15.0 ± 6.8	-42.6 ± 10.4	26.6 ± 8.9
σ	62.1 ± 4.9	64.5 ± 4.9	68.5 ± 5.8	66.4 ± 5.9	72.3 ± 4.8	70.4 ± 4.8	86.3 ± 7.3	77.1 ± 6.3
Median	-21.4	-9.9	61.4	16.8	9.5	23.1	-51.2	22.6
	Near ($N = 9590$):				Far ($N = 7349$):			
Mean	-17.0 ± 1.0	-5.9 ± 1.0	60.4 ± 0.7	0.6 ± 0.8	-2.7 ± 1.0	8.1 ± 1.1	-57.7 ± 0.8	-0.2 ± 0.8
σ	74.0 ± 0.7	72.0 ± 0.7	49.4 ± 0.5	51.9 ± 0.5	61.3 ± 0.7	63.8 ± 0.7	46.8 ± 0.6	49.2 ± 0.6
Median	-21.7	-10.3	56.4	0.9	1.5	13.4	-54.5	-0.7

a Toomre- $Q = 1.2$ and is immersed in an isothermal halo with scale-length $r_h = 3.3R_d$. The model has 7.5×10^6 particles; it was evolved on a cylindrical grid code described in Sellwood & Valluri (1997). The model forms a bar and experiences a violent buckling instability leading to the formation of a B/P shape. The formation of the B/P shape is presented as an animation in Debattista et al. (2006) (where it is referred to as model L2).

In order to compare the model with the Milky Way, we need to rescale from natural units in which $R_d = M_d = G = 1$ (where M_d is the disc mass) to physical units and rotate the model to reproduce the observed inclination bar in the Galaxy. To scale sizes, we use units of the bar radius, placing the observer at two bar radii from the centre of the galaxy, with the bar extending to $\sim 1.45R_d$ of the initial disc. We scale velocities by multiplying the unit velocity by 250 km s^{-1} . The bar in the model was rotated to an angle of 20 degrees relative to the Sun-Galactic centre direction. We selected particles from both sides of the center of the model, at an observing window of $(l, b) = (0, -6)$. The selection of particles was done based on their spatial distribution along the x coordinate. Two overdensities were observed, corresponding with the two arms of the “X” (B/P-shape). Around each peak, Near and Far samples were defined in order to better represent the position of the clumps, avoiding background and foreground contamination. Figure 7 shows a qualitative comparison between the observations and the model, in which the median values for the BRC/Near and FRC/Far samples and in particular their differences are consistent. Table 1 shows the mean, dispersion and median for each velocity component present in Fig. 7. As is possible to observe, most of the velocities predicted by the model are consistent with the observed ones (within the errors) except for W, which is hotter than the model in $\sim 20 \text{ km/s}$. A mismatch in the specific value of the mean and dispersion for the velocity distributions (instead the difference) are not unexpected, due the model has not been built particularly for the Milky Way. Additional analysis will be presented in Gardner et al. (in prep).

It is worth emphasizing that this consistency of our data with the model does not necessarily prove that the model fully represent the formation history of the MW bulge. Indeed, in this class of purely N-body models (e.g., Debattista et al. 2006; Shen et al. 2010) the gas contribution of the overall event of bulge formation is not taken into account. Instead, when the bulk of the bulge stars formed, some $\sim 10 \text{ Gyr}$ ago, the Galaxy was likely to be very gas rich, with a gas fraction of $\sim 50\%$, as indicated by direct observations of star forming galaxies at the corresponding lookback time (i.e., at $z \approx 2$, see Tacconi et al. 2010; Daddi, et al. 2010).

6. Metallicity distribution

Calcium II Triplet (CaT) metallicities for both the IMACS and the GIRAFFE spectra have been derived using the calibration by Vásquez et al. (in prep). The latter has been constructed by observing a sample of RC and RGB stars in Baade’s Window, with the GIRAFFE spectrograph, in the LR08 setup, centered at 8817 \AA . GIRAFFE high resolution spectra had been previously obtained for the same stars by our group, and $[\text{Fe}/\text{H}]$ measurements based on such spectra are presented in Hill et al. (2011). The comparison between the equivalent widths (EWs) of CaT lines in the LR08 spectra and the $[\text{Fe}/\text{H}]$ abundances, obtained from the EWs of individual FeI lines, yields a linear relationship that extends up to $[\text{Fe}/\text{H}] \sim +0.5 \text{ dex}$, and it is fully compatible with the analogous relations obtained by Cole et al. (2004) and Warren et al. (2009). The details of the new calibration will be discussed in a separate paper. We emphasize here that it has been constructed precisely for bulge giants and particularly tested for RC stars.

In order to convert EWs into metallicities it is necessary to calculate the so called *reduced* EWs, a parametrization that removes the effects of temperature and gravity on the EWs, defined as

$$W' = \Sigma EW + \beta(K - K_{RC}), \quad (3)$$

where K_{RC} is the mean K_s magnitude of the RC. In our case, K_{RC} was obtained independently for the bright and faint RC using the photometric catalogue from the VVV survey (Saito et al. 2012) and extinction maps from Gonzalez et al. (2012). The quantity ΣEW is the sum of the EWs of the three calcium lines. The measurement of the EWs of CaT lines is rather difficult for stars of solar and super-solar metallicity, due to the presence of many small molecular lines that contaminate the *pseudo*-continuum. In the case of IMACS spectra the task is further complicated by the fact that the dispersion axis goes across 4 different chips of the mosaic, with gaps between them. For this reason, as well as due to lower S/N of the IMACS spectra with respect to the GIRAFFE ones used to derive the calibration, the metallicity derived from IMACS spectra are not very accurate. In particular, for four stars in common between the IMACS and GIRAFFE samples, the derived metallicities show both an offset (of $\sim 0.2 \text{ dex}$) with a mild trend with metallicity. Rather than relying on just four stars to measure and correct for this systematics, we prefer to analyse here only the metallicities for the IMACS targets, without combining them with the GIRAFFE ones.

One might argue that we are ignoring the highest quality data (GIRAFFE sample) keeping only the lower quality ones (IMACS sample). This choice is due to the larger number of IMACS targets, and it is justified by the assumption that the impact of the systematics in the measurements of EWs in IMACS

would be small, if metallicities are considered only in a *relative* scale. The IMACS metallicities will be labelled as *instrumental*, hereafter, in order to emphasize that we have indications that they might not be accurate, in an absolute scale. Moreover, these CaT metallicities are used uniquely to check whether the bright and faint clumps have consistent or (slightly) different metallicity distributions.

Figure 8 shows the metallicity histogram for the target stars in the bright (red) and the faint RC (blue). As already found by de Propris et al. (2011), the two samples do not show any difference in their mean metallicity. However, if we select only bright RC stars with $V_R < -50$ km/s and faint RC stars with $V_R > +50$ km/s, as already done for the PMs, then a difference of ~ 0.11 dex is found between the mean $[\text{Fe}/\text{H}]$ of the two samples. A small difference between the near and the far overdensities of bulge stars at $(l, b) = (0, -6)$ is consistent with the presence of a gradient along the minor axis, as observed by Zoccali et al. (2008), Johnson et al. (2011), and Gonzalez et al. (2011). Indeed, the line of sight crosses the near and the far overdensities at different distances from the Galactic center. In order to estimate the expected difference in metallicity, the distance to each overdensity was determined following McWilliam & Zoccali (2010), finding a $\Delta Z \sim 200$ pc in their distance to the Galactic plane. Assuming a 0.6 dex/kpc gradient, a difference of 0.12 dex in metallicity would be expected between stars in the two RCs. Clearly, this comparison is very preliminary, because the radial velocity cut is arbitrary, and because the gradient quoted in the literature is based on samples of stars without line of sight distance information, i.e., summing up -in an unknown proportion- stars in the near and far overdensities. In summary, there is evidence, in the literature, of the presence of a metallicity gradient along the bulge minor axis. While the value of this gradient is quite uncertain, here we found that adopting a radial velocity cut that minimizes cross contamination a metallicity gradient appears that is consistent with that reported by Zoccali et al. (2008).

Finally, another interesting piece of evidence is shown in Figure 9. The metallicity of the bright (red) and faint (blue) RC stars is shown here as a function of RV. A glance at this plot shows some segregation of the faint RC stars on the right half of the plane, while the bright RC ones are preferentially on the left side. The additional evidence appearing here is that this segregation is stronger for metal poor stars ($[\text{Fe}/\text{H}] < 0$), shown in the lower left panel, than it is for the metal rich ones ($[\text{Fe}/\text{H}] > 0$), shown in the lower right panel. Surprisingly, this would argue in favor of the metal poor stars being preferentially in the more elongated orbits, defining the X-shape, while the most metal rich ones are preferentially found on axisymmetric orbits, centered at zero RV and with lower velocity dispersion.

Ness et al. (2012) also found that metal rich RC stars have smaller velocity dispersion than metal poor ones, consistent with what we see in Fig. 8. They also found that the magnitude (distance) separation between the two RCs is stronger for metal rich stars. The latter evidence cannot be checked here because our initial target selection excluded stars in between the two RCs. Our results that the radial velocity asymmetry is stronger for the metal poor half of the sample, however, suggests that the magnitude splitting should be there, perhaps even stronger, for these stars.

7. Conclusions

We have analysed a sample of 454 bulge stars equally distributed between the bright and the faint RCs of a bulge field

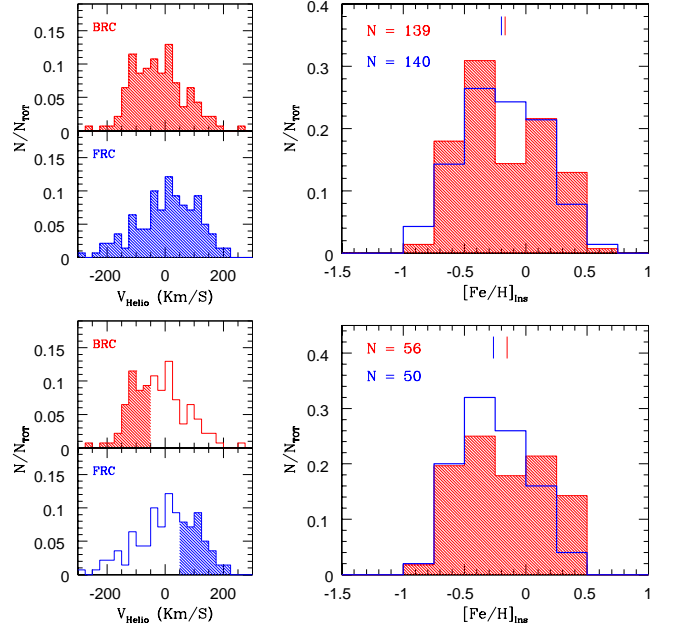


Fig. 8. Instrumental metallicity distribution for IMACS data. Selecting all the BRC and FRC in whole RV regime (upper-left panels), the $[\text{Fe}/\text{H}]_{\text{Ins}}$ distribution plotted in upper-right panel do not show a statistical difference. Nevertheless when a selection is done in the same way as Figure 6 (lower-left panels), a shift in the $[\text{Fe}/\text{H}]_{\text{Ins}}$ distribution is observed in lower-right panel. The star number is also indicated in each case following the key color adopted in this paper and the corresponding selection showed in left panels.

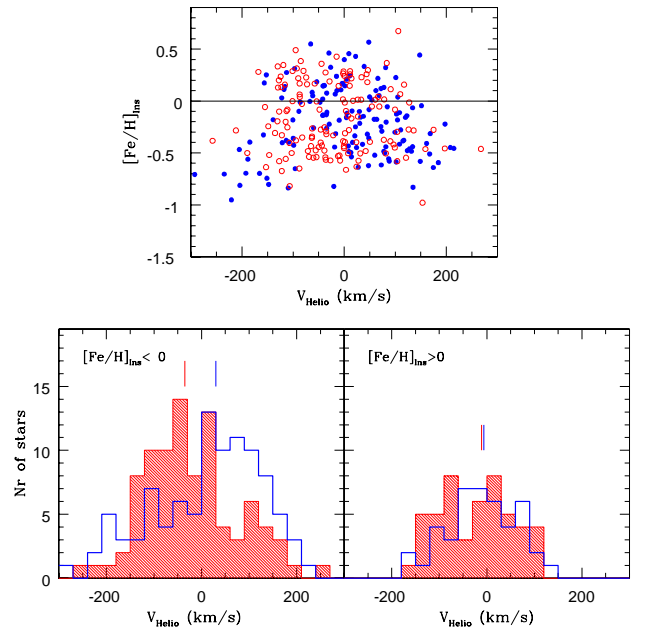


Fig. 9. $[\text{Fe}/\text{H}]$ versus RV for BRC and FRC samples observed with IMACS. The histograms show an interesting difference when the sample is divided in metal poor and metal rich.

at $(l, b) = (0, -6)$. The two RCs are used here as tracers of the near and far overdensities of the X-shaped bulge, crossed by the line of sight at these coordinates. We obtained radial velocities and proper motions for all the stars, and CaT metallicities for a subsample of 352 stars.

We also measured the proper motion of NGC 6558, finding an observed mean proper motion of $(\mu_l \cos(b), \mu_b) = (0.30 \pm 0.14, -0.43 \pm 0.13)$, with a dispersion of $(\sigma_l \cos(b), \sigma_b) = (1.8, 1.7)$ mas/yr. This is the first PM measurement for NGC 6558.

An excess of bulge stars in elongated orbits ($|V_R| > 50$ km/s) has been found in both RCs, with the near overdensity containing preferentially stars with negative RVs, while the far one contains preferentially stars with positive RVs. The 3D velocities of these stars are qualitatively consistent with the predictions of N -body models by Debattista et al. (2005) with a strong X-shaped bulge.

Interestingly, not all the stars in the two RCs are in elongated orbits. Roughly half of the stars in both the bright and the faint RC share the same 3D velocity, with mean RVs and PMs centered at zero. They seem to be stars in axisymmetric orbits that are somehow coexisting with those in elongated orbits. Whether the two kinematic groups share the same origin, i.e., they both belong to the same Galactic component is impossible to say with the present data. Nevertheless, it is interesting to note that current models predict that the presence of a bar should clean up the inner region of a Galaxy, i.e., no stars in axisymmetric orbits should be left there, regardless of their origin.

Metallicity measurements provide further some evidence for the stars in elongated orbits, i.e., those with the largest difference in RV and PMs, being preferentially the ones with sub-solar metallicities, while the more metal rich ones in both the near and far overdensity share the same 3D motions, with RV and PMs centered at zero, and a smaller radial velocity dispersion. This finding, if confirmed, would be at odds with the suggestion by Babusiaux et al. (2010) that metal poor bulge stars have spheroid-like kinematics, while the metal rich ones have a significant vertex deviation, typical of stars in bar-like orbits.

Clearly, all the evidence presented here is based on a relatively small number of stars, and needs to be confirmed with larger samples, such as the ESO–Gaia Public Spectroscopic Survey (PIs: Gilmore & Randich), the ARGOS survey (PI: Freeman), ESO Large Programme 187.B-0909 (PI: Zoccali) and the APOGEE survey (PI: Majewski). Indeed, the present pilot study demonstrates the amount of information that can be acquired by combining spectra with multiepoch photometry for red clump stars, for which distances are known. For example, with the ESO Large Programme we expect to soon be able to use this kind of data for significantly larger samples of stars along many different bulge lines of sight. As a result, important constraints will be set to state of the art dynamical models, with the ultimate aim of establishing the relative roles of the processes that contributed to make the Milky Way bulge as we see it today.

Acknowledgements. We thank Santino Cassisi for calculating the expected fraction of red giant branch contamination in the red clump, from his models. SV and MZ acknowledge support by Proyecto Fondecyt Regular 1110393. While working at this paper, MZ enjoyed a sabbatical year at the INAF Osservatorio Astronomico di Bologna, and the European Southern Observatory in Garching. Both institutions are warmly thanked for their kind hospitality. A fellowship from the John Simon Guggenheim Memorial Foundation has partly financed this stay. This work is supported by the BASAL Center for Astrophysics and Associated Technologies PFB-06, the FONDAP Center for Astrophysics 15010003, Proyecto Anillo ACT-86 and by the Chilean Ministry for the Economy, Development, and Tourism's Programa Iniciativa Científica Milenio through grant P07-021-F, awarded to The Milky Way Millennium Nucleus.

MM was supported by the IAC (grants 310394, 301204), the Education and Science Ministry of Spain (grants AYA2010-16717).

References

- Anderson, J., Bedin, L. R., Piotto, G., et al. 2006, *A&A*, 454, 1029
 Athanassoula, E. 2005, *MNRAS*, 358, 1477
 Athanassoula, E. 2003, *MNRAS*, 341, 1179
 Athanassoula, E. 2012, *MNRAS* in press (astro-ph/1207.4590)
 Babusiaux, C. & Gilmore, G. 2005, *MNRAS*, 358, 1309
 Babusiaux, C., Gómez, A., Hill, V., et al. 2010, *A&A*, 519, A77
 Barbuy, B., Zoccali, M., Ortolani, S., et al. 2007, *AJ*, 134, 1613
 Binney, J., Gerhard, O., Spergel, D. 1997, *MNRAS*, 288, 365
 Bissantz, N. & Gerhard, O. 2002, *MNRAS*, 330, 591
 Bournaud, F., Elmegreen, B. G., & Martig, M. 2009, *ApJ*, 707, L1
 Cabrera-Lavers, A., Hammersley, P. L., González-Fernández, C., et al. 2007, *A&A*, 465, 825
 Cabrera-Lavers, A., González-Fernández, C., Garzón, F., et al. 2008, *A&A*, 491, 781
 Carollo, C. M., Scarlata, C., Stiavelli, M., et al. 2007, *ApJ*, 658, 960
 Churchwell, E., Babler, B. L., Meade, M. R., et al. 2009, *PASP*, 121, 213
 Clarkson, W., Sahu, K., Anderson, J., et al. 2008, *ApJ*, 684, 1110
 Clarkson, W. I., Sahu, K.C., Anderson, J. et al. 2011, *ApJ*, 735, 37
 Cole A. A., Smecker-Hane T. A., Tolstoy E., et al. 2004, *MNRAS*, 347, 367
 Combes, F., & Sanders, R.H. 1981, *A&A*, 96, 164
 Daddi, E., Bournaud, F., Walter, F., et al. 2010, *ApJ*, 713, 686
 De Propriis, R., Rich, R. M., Kunder, A., et al. 2011, *ApJ*, 732, L32
 Debattista, V. P., Carollo, C. M., Mayer, L., et al. 2005, *ApJ*, 628, 678
 Debattista, V. P., Mayer, L., Carollo, C. M., et al. 2006, *ApJ*, 645, 209
 Dehnen, W. & Binney, J. J. 1998, *MNRAS*, 298, 387
 Dehnen, W. 2000, *AJ*, 119, 800
 Dwek, E., Arendt, R. G., Hauser, M. G., et al. 1995, *ApJ*, 445, 716
 Elmegreen, B. G., Bournaud, F., & Elmegreen, D. M. 2008, *ApJ*, 688, 67
 Emsellem, E., Cappellari, M., Krajnović, D., et al. 2011, *MNRAS*, 414, 888
 Feltzing, S. & Johnson, R. A. 2002, *A&A*, 385, 67
 Förster Schreiber, N.M., Genzel, R., Lehnert, M. D., et al. 2006, *ApJ*, 645, 1062
 Genzel, R.; Newman, S.; Jones, T., et al. 2011, *ApJ*, 733, 101
 Gonzalez, O. A., Rejkuba, M., Zoccali, M., et al. 2011, *A&A* 530, A54
 Gonzalez, O. A., Rejkuba, M., Zoccali, M., et al. 2012, *A&A*, 543, A13
 Hammersley, P. L., Garzón, F., Mahoney, T. J., et al. 2000, *MNRAS*, 317, L45
 Hanuschik, R. W. 2003, *A&A*, 407, 1157
 Harris, W.E. 1996, *AJ*, 112, 1487
 Hill, V., Lecureur, A., Gómez, A., et al. 2011, *A&A*, 534, A80
 Howard, C. D.; Rich, R. M.; Reitzel, D. B., et al. 2008, *ApJ*, 688, 1060
 Howard, C. D., Rich, R. M., Clarkson, W., et al. 2009, *ApJ*, 702, L153
 Immeli, A., Samland, M., Gerhard, O., & Westera, P. 2004, *A&A*, 413, 547
 Johnson, D. R. H. & Soderblom, D. R. 1987, *AJ*, 93, 864
 Johnson, C. I., Rich, R. M., Fulbright, J. P., et al. 2011, *ApJ*, 732, 108
 Kent, S. M. 1992, *AJ*, 104, 387, 181
 Kuijken, K. & Rich, R. M. 2002, *AJ*, 124, 2054
 Kunder, A., Koch, A., Rich, R. M., et al. 2012, *AJ*, 143, 57
 López-Corredoira, M., Cabrera-Lavers, A., Mahoney, T. J., et al. 2007, *AJ*, 133, 154
 Martínez-Valpuesta, I., Shlosman, I. & Heller, C. 2006, *ApJ*, 637, 214
 Martínez-Valpuesta, I. & Gerhard, O. 2011, *ApJ*, 734, L20
 McWilliam, A. & Zoccali, M. 2010, *ApJ*, 724, 1491
 Minniti, D. 1996, *ApJ*, 459, 175
 Nataf, D. M., Udalski, A., Gould, A., et al. 2010, *ApJ*, 721, L28
 Ness, M., Freeman, K., Athanassoula, E., et al. 2012, *ApJ*, 756, 22
 Ortolani, S., Renzini, A., Gilmozzi, R. et al. 1995, *Nature*, 377, 701
 Patsis, P. A., Skokos, Ch. & Athanassoula, E. 2002, *MNRAS*, 337, 578
 Pryor, C. & Meylan, G. 1993, *ASPC*, 50, 357
 Rangwala, N., Williams, T. B. & Stanek, K. Z. 2009, *ApJ*, 691, 1387
 Rangwala, N. & Williams, T. B. 2009, *ApJ*, 702, 414
 Rattenbury, N. J., Mao, S., Sumi, T., et al. 2007, *MNRAS*, 378, 1064
 Rich, R. M. 1988, *AJ*, 95, 828
 Rich, R. M. 1990, *ApJ*, 362, 604
 Rich R. M. & Terndrup D. 1997, *ASPC*, 127, 129
 Roeser, S., Demleitner, M. & Schilbach, E. 2010, *AJ*, 139, 2440
 Robin, A. C., Reyle, C., Derriere, S., et al. 2003, *A&A*, 409, 523
 Robin, A. C., Marshall, D. J., Schultheis, M., et al. 2012, *A&A*, 538, A106
 Sadler, E. M., Rich, R. M. & Terndrup, D. M. 1996, *AJ*, 112, 171
 Saha, K., Martínez-Valpuesta, I., & Gerhard, O. 2012, *MNRAS*, 421, 333
 Saha, K., Tseng, Y., & Taam, R.E. 2010, *ApJ*, 721, 1878
 Saito, R., Zoccali, M., McWilliam, A., et al. 2011, *AJ*, 142, 76
 Saito, R. K., Hempel, M., Minniti, D., et al. 2012, *A&A*, 537, A107
 Sellwood, J. A., & Valluri, M. 1997, *MNRAS*, 287, 124

- Schönrich, R., Binney, J. and Dehnen, W. 2010, MNRAS, 403, 1829
Scott D. W. 1985, The Annals of Statistics, 13, 1024
Shen, J., Rich, R.M., Kormendy, J. et al. 2010, ApJ, 720, L72
Skrutskie, M.F., Cutri, R.M., Stiening, R., et al. 2006, AJ, 131, 1163
Soto, M., Rich, R. M. & Kuijken, K. 2007, ApJ, 665, L31
Spaenhauer, A., Jones, B. F. & Whitford, A. E. 1992, AJ, 103, 297
Stanek, K. Z., Mateo, M., Udalski, A., et al. 1994, ApJ, 429, L73
Stetson, P. B. & Harris, W. E. 1988, AJ, 96, 909
Stetson P. B. 1994, PASP, 106, 250
Sumi, T., Wu, X., Udalski, A., et al. 2004, MNRAS, 348, 1439
Szymanski, M. K., Udalski, A., Soszynski, I., et al. 2011, AcA, 61, 83
Tacconi, L. J., Genzel, R., Neri, R., et al. 2010, Nature, 463, 781
Taylor, M. B., 2005, in "Astronomical Data Analysis Software and Systems",
XIV ASP Conference Series, eds Shopbell, P., Britton M. & Ebert, R., (San
Francisco, ASP), vol. 347, p. 29
Terndrup, D. M., Sadler, E. M. & Rich, R. M. 1995, AJ, 110, 1774
Toomre, A. 1977, in Evolution of Galaxies and Stellar Populations, edited by
B.M. Tinsley & R.B. Larson (New Haven: Yale University Observatory, p.
401
Uttenhaler, S., Schultheis, M., Nataf, D. M., et al. 2012, A&A, 546, A57
Vieira, K., Casetti-Dinescu, D., Mendez, R., et al. 2007, AJ, 134, 1432
Warren, Steven R. & Cole, Andrew A. 2009, MNRAS, 393, 272
Zacharias, N. 2010, AJ, 139, 2184
Zhao, H.S. 1996, MNRAS, 283, 149
Zoccali, M., Renzini, A., Ortolani, S., Bica, et al. 2001, AJ, 121, 2638
Zoccali, M., Renzini, A., Ortolani, S., et al. 2003, A&A, 399, 931
Zoccali, M., Hill, V., Lecureur, A., et al. 2008, A&A, 486, 177